Check for updates

ADVANCED SCIENCE Open Access
www.advancedscience.com

Ferroelectric Orthorhombic ZrO_2 Thin Films Achieved Through Nanosecond Laser Annealing

Anna P. S. Crema, Marian C. Istrate, Alexandre Silva, Veniero Lenzi, Leonardo Domingues, Megan O. Hill, Valentin S. Teodorescu, Corneliu Ghica, Maria J. M. Gomes, Mario Pereira, Luís Marques, Judith L. MacManus-Driscoll, and José P. B. Silva**

A new approach for the stabilization of the ferroelectric orthorhombic ZrO_2 films is demonstrated through nanosecond laser annealing (NLA) of as-deposited Si/SiO_x/W(14 nm)/ZrO_2(8 nm)/W(22 nm), grown by ion beam sputtering at low temperatures. The NLA process optimization is guided by COMSOL multiphysics simulations. The films annealed under the optimized conditions reveal the presence of the orthorhombic phase, as confirmed by X-ray diffraction, electron backscatter diffraction, and transmission electron microscopy. Macroscopic polarization-electric field hysteresis loops show ferroelectric behavior, with saturation polarization of 12.8 µC cm^{-2}, remnant polarization of 12.7 µC cm^{-2} and coercive field of 1.2 MV cm^{-1}. The films exhibit a wake-up effect that is attributed to the migration of point defects, such as oxygen vacancies, and/or a transition from nonferroelectric (monoclinic and tetragonal phase) to the ferroelectric orthorhombic phase. The capacitors demonstrate a stable polarization with an endurance of 6.0×10^5 cycles, demonstrating the potential of the NLA process for the fabrication of ferroelectric memory devices with high polarization, low coercive field, and high cycling stability.

1. Introduction

Ferroelectrics research field has rejuvenated in the last decade due to the discovery of ferroelectricity in simple binary or ternary fluorite-based oxide thin films.[1]

The interest in these materials arises from their compatibility with complementary metal-oxide semiconductors (CMOS) where high-temperature-grown perovskites present more challenges. Hence, compared to conventional perovskites, they have a lower temperature of fabrication as well as high scalability potential. Thus, these fluorite-based films could solve the energy efficiency problem of scaled semiconductors in a number of ways, e.g. when used in ferroelectric capacitors, transistors or tunnel junctions, negative capacitance devices, logic-in-memory, neuromorphic computing. Other energy storage, pyroelectric or piezoelectric-based applications are also possible.[1,2]

In 2011, Böscke et al. reported for the first time on the ferroelectric properties of Si-doped HfO_2 thin films.[3] Many research groups followed this path and investigated several other dopants such as La, Gd, Y, Al, etc, either in polycrystalline or epitaxial films.[4,5,6,7]

Due to the possibility of achieving a wide range of properties ranging from dielectric to ferroelectric and antiferroelectric, $Hf_xZr_{1-x}O_2$ (HZO), with x from 0 up to 1, is a very promising composition compared to other doped HfO_2 compositions

A. P. S. Crema, A. Silva, V. Lenzi, L. Domingues, M. J. M. Gomes, M. Pereira, L. Marques, J. P. B. Silva
Physics Center of Minho and Porto Universities (CF-UM-UP)
University of Minho
Campus de Gualtar, Braga 4710-057, Portugal
E-mail: josesilva@fisica.uminho.pt

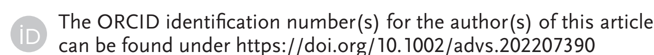
The ORCID identification number(s) for the author(s) of this article can be found under https://doi.org/10.1002/advs.202207390

© 2023 The Authors. Advanced Science published by Wiley-VCH GmbH. This is an open access article under the terms of the Creative Commons Attribution License, which permits use, distribution and reproduction in any medium, provided the original work is properly cited.

DOI: 10.1002/advs.202207390

A. P. S. Crema, A. Silva, V. Lenzi, L. Domingues, M. J. M. Gomes, M. Pereira, L. Marques, J. P. B. Silva
Laboratory of Physics for Materials and Emergent Technologies
LapMET
University of Minho
Braga 4710-057, Portugal

M. C. Istrate, V. S. Teodorescu
University of Bucharest
Faculty of Physics
Atomistilor 405, Magurele, Ilfov 077125, Romania

M. C. Istrate, V. S. Teodorescu, C. Ghica
National Institute of Materials Physics
Lab. of Atomic Structures and Defects in Advanced Materials
405A Atomistilor Str., Magurele, Ilfov 077125, Romania

M. O. Hill, J. L. MacManus-Driscoll
Dept. of Materials Science and Metallurgy
University of Cambridge
27 Charles Babbage Rd, Cambridge CB3 OFS, United Kingdom
E-mail: jld35@cam.ac.uk

21983844, 2023, 15, Downloaded from https://onlinelibrary.wiley.com/doi/10.1002/advs.202207390 by Cochrane Portugal, Wiley Online Library on [26/07/2023]. See the Terms and Conditions (https://onlinelibrary.wiley.com/terms-and-conditions) on Wiley Online Library for rules of use; OA articles are governed by the applicable Creative Commons License

because it gives the possibility of using these materials in nonvolatile memory devices and energy storage capacitors.[1,8,9] Dopant concentration, strain, electrode materials, and the upper capping layer are all reported to influence the polymorphism in HZO films.[10,11,12] One of the most promising strategies used to stabilize the orthorhombic (*o*-) phase and enhance the ferroelectric properties of HZO films was the use of tensile stress.[13,14,15] Different tensile stress levels can be obtained by the appropriate choice of the electrodes, since the difference in the thermal expansion coefficient (TEC) of HZO and the electrode is one of the important origins of tensile stress when the films are cooled down to room temperature.

Different electrode materials such as TiN,[16,17,18] Pt,[17] W,[17] $La_{0.67}Sr_{0.33}MnO_3$6, $Pb_2Ir_2O_7$,[18] etc. have been investigated. Among them, TiN is widely used as an electrode to induce ferroelectricity in HZO-based capacitors. However, it has a high TEC (9.1×10^{-6} K^{-1}) comparable with that of HZO film (10×10^{-6} K^{-1}),[15] which is not beneficial for the suppression of nonferroelectric (i.e., *c*, *t*, and *m*) phases, resulting in relatively low ferroelectric polarization. In this context, tungsten (W) emerges as the best choice since it exhibits the lowest TEC (4.5×10^{-6} K^{-1})[19] that allows to achieve high polarization values. However, *W* is a reactive metal that could easily react with oxygen in the HZO layer, leading to the formation of WO_x layer that can degrade the device performance.[20]

Although HZO shows the largest polarisation values, ZrO_2 is much more abundant in nature and therefore is a more appealing choice for large-scale use.[21] The emergence of the ferroelectricity in ZrO_2 arises from the *o*-phase (space group: $Pca2_1$)[22] and the polar rhombohedral *(r-)*phase (space group: R3m)[23] that can be only achieved in a constrained environment in the thin film form. It was recently revealed that ferroelectricity and hysteretic polarization switching can be achieved in ultrathin ZrO_2 with the fluorite-structure unit-cell size[24] for a film thickness of 5 Å. However, pure ZrO_2 films have shown a moderate polarization,[23] in spite of the theoretical predictions that point to a high polarization value close to the one observed in doped HfO_2.[25] Therefore, ZrO_2 thin films require further optimization. However, to the best of our knowledge the potential use of W electrodes to fabricate ferroelectric devices based on ZrO_2 thin films was not yet investigated in spite of the TEC coefficient of ZrO_2 (10.5×10^{-6} K^{-1})[26] is very similar to the ones of HfO_2 and HZO and significantly higher than the one from W (4.5×10^{-6} K^{-1}).[19]

In this context, the use of W electrodes to promote the formation of the *o*-phase with improved ferroelectric performance is investigated in this study. We first grew $W/ZrO_2/W$ structures onto Si/SiO_x substrates by ion beam sputtering at a maximum temperature of 330 °C. We then performed the crystallization of the ZrO_2 layer by nanosecond laser annealing (NLA). This was done by implementing a simulation-guided approach to determine the appropriate NLA conditions. It was previously reported the successful use of the NLA process to promote the fabrication of Si-doped HfO_2 and HZO capacitors,[27–29] but the use of NLA to promote the crystallization of the ZrO_2 films has not previously been investigated. As well as being advantageous for producing rapid crystallization, compared to standard annealing NLA can strongly reduce W oxidation as the annealing time is very short, in the ns range. Overall, we provide experimental evidence for the formation of the *o*-phase in the ZrO_2 films in the $Si/SiO_x/W/ZrO_2$ film stack and we demonstrate stable ferroelectric performance.

2. Experimental Section

2.1. Device Fabrication and Characterization

W(14 nm)/ZrO_2(8 nm)/W(22 nm) structures were grown by ion-beam sputter deposition (IBSD) onto p-type (100) Si/SiO_x substrates (Si-Mat). The IBSD chamber is equipped with a multi-target carousel system that allows the deposition of the bottom W and ZrO_2 layers without breaking the vacuum. The vacuum chamber was first evacuated down to a low pressure of 1×10^{-6} mbar prior to the deposition. During the deposition, the substrate was kept at a temperature of 22 °C and 330 °C for W and ZrO_2, respectively, at a distance of 87.3 mm from the target. The gas pressure inside the chamber was maintained constant at 2.5×10^{-4} mbar. A gas flow of 8.0 ml min^{-1} of Ar was introduced into the ion beam gun and the atoms were ionized in the ion source with an RF-power of 100 W. The ion beam was further accelerated at 500 V and 600 V for W and ZrO_2, respectively, and the ion beam current was maintained at 13 and 14 mA, respectively. Then, for the top W electrode deposition a shadow mask was used to pattern circular electrodes, with 0.8 mm diameter. After the deposition of the structures, nanosecond laser annealing was performed in air, at room temperature, using a KrF laser ($\lambda = 248$ nm). The laser, with an energy density of ≈0.4 J cm^{-2}, was emitting light with a pulse length of 25 ns, and a repetition rate of 10 Hz, during 10 s (100 pulses). The spot size of the laser is 10×5 mm^2, which is large enough when compared to the device size in order to have a uniform annealing.

The structural characterization of the deposited layers was performed using X-ray diffraction (XRD), which was carried out in a Bruker D8 Advance DaVinci (Germany) diffractometer at room temperature over the $2\bar{e}$ range = 22–36°, in a Bragg-Brentano configuration using CuKα radiation ($\lambda = 1.5406$ Å). The microstructural characterization of the sample was performed by high-resolution transmission electron microscopy (HRTEM) using a JEM ARM200F instrument operated at 200 kV. The cross-section TEM specimen was prepared for analysis by mechanical polishing down to ≈30 µm, followed by ion milling in a Gatan PIPS machine at 4 kV accelerating voltage and 7° incidence angle. Low-voltage ion milling was used as a final polishing stage in order to reduce the amorphous surface layer enveloping the specimen. Electron backscatter diffraction (EBSD) was performed using a ZEISS GeminiSEM 300 at accelerating voltages between 15 and 20 kV and a beam aperture between 60 and 120 µm. Electron backscatter patterns (EBSPs) were collected on an Oxford instruments Symmetry S3 CMOS-based detector. Films were grounded for EBSD measurements using Ag paste. Ferroelectric hysteresis loops (*P-E*) were measured at room temperature with a modified Sawyer-Tower circuit using a triangular signal of 0.5, 1, and 2.5 kHz.

2.2. Computational Simulation

Figure 1 shows the geometry of the $W/ZrO_2/W$/Si(substrate) and the 2D axisymmetric domain used in the simulations of ns-laser

 © 2023 The Authors. Advanced Science published by Wiley-VCH GmbH

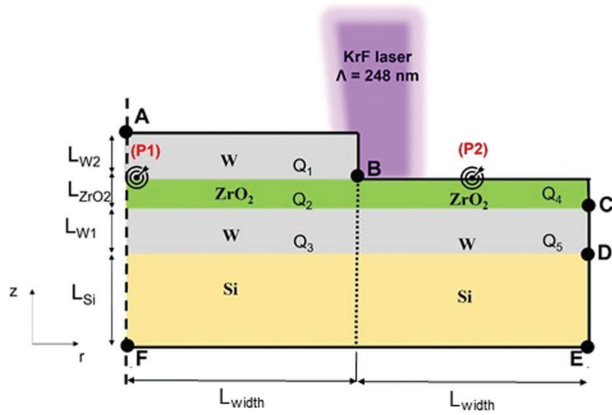

Figure 1. Simulated schematic view of boundary conditions of laser beam interaction with material layers. P1: ZrO_2 surface under W electrode. P2, ZrO_2 surface exposed to air.

annealing multilayer stack. For simplicity, we neglected the existence of the native SiO_x layer. The COMSOL Multiphysics software was used to perform the simulations of the laser heating and heat transport in the multilayer stack by solving the nonlinear inhomogeneous heat conduction equation,

$$\rho(T)\,c(T)\,\frac{\partial T(r,z,t)}{\partial t} = \nabla\cdot\left[k(T)\,\vec{\nabla}T(r,z,t)\right] + Q(r,z,t) \tag{1}$$

where $T(r,z,t)$ is the temperature, ρ is the density, c is the specific heat, k is the thermal conductivity of the material. The term $Q(r,z,t)$ is the volumetric heat source due the absorption of incident laser radiation by the material. Using the Beer–Lambert law and assuming that the laser radiation intensity is uniformly distributed over the irradiated area, $Q(r,z,t)$ can be expressed as:

$$Q\ (r,z,t) = \alpha(T)\,(1-R(T))\,q(t)\,exp\left(-\int_0^z \alpha(T)\,dz'\right) \tag{2}$$

with α is the material absorption coefficient, R as its reflection coefficient, and $q(t)$ is the laser pulse temporal profile, described by

$$q\ (t) = \frac{W}{\tau}\sin^2\left(\frac{\pi t}{2\tau}\right) \tag{3}$$

where W represents the laser energy density and τ is the half amplitude of the pulse duration. The volumetric heating source terms Q_{1}-$_5$ for the different layers in Figure 1 are written as:

$$Q_1 = \alpha_W q(t)\left(1-R_W\right)e^{-\alpha_W\times\left(L_{tot}-z\right)} \tag{4}$$

$$Q_2 = \alpha_{ZrO2} q(t)\left(1-R_W\right)e^{-\alpha_W\times L_{W2}}e^{-\alpha_{ZrO2}\times\left(L_{tot}-L_{W2}-z\right)} \tag{5}$$

$$Q_3 = \alpha_W q(t)\left(1-R_W\right)e^{-\alpha_W\times L_{W2}}e^{-\alpha_{ZrO2}\times L_{ZrO2}}e^{-\alpha_{W2}\times\left(L_{tot}-L_{W2}-L_{ZrO2}-z\right)} \tag{6}$$

$$Q_4 = \alpha_{ZrO2} q(t)\left(1-R_{ZrO2}\right)e^{-\alpha_{ZrO2}\times\left(L_{tot}-L_{W2}-z\right)} \tag{7}$$

$$Q_5 = \alpha_W q(t)\left(1-R_W\right)\left(1-R_{ZrO2}\right)e^{-\alpha_{ZrO2}\times L_{ZrO2}} \times e^{-\alpha_{W2}\times\left(L_{tot}-L_{W2}-L_{ZrO2}-z\right)} \tag{8}$$

To solve Equation (1), suitable boundaries and initial conditions were defined. The initial temperature of the multilayer stack was set in the computational model to the room temperature:

$$T(r,z,t=0) = T_{\text{amb}}. \tag{9}$$

where T_{amb} is the ambient temperature, 293,15 K. This fixed temperature assumption was also used for the Si substrate bottom surface ($\underline{EF}$):

$$T(r,z=0,t) = T_{\text{amb}} \tag{10}$$

For $\underline{AF}$ surface, the axial symmetry boundary condition was considered:

$$\frac{dT}{dr} = 0 \tag{11}$$

The boundary conditions for surfaces $\underline{AB}$, $\underline{BC}$, $\underline{CD}$, $\underline{DE}$, consider radiation heat losses to the ambient using the Stefan-Boltzmann law:

$$-n\cdot\left(k\vec{\nabla}T\right) = \sigma\varepsilon\left(T^4 - T_{\text{amb}}^4\right) \tag{12}$$

where n is the surface normal vector, ϵ is the surface emissivity, σ is the Stefan-Boltzmann constant. We also assume a perfect thermal contact between the W/ZrO_2/W/Si layers and neglect the interface thermal resistance effect.

The heat transfer module of COMSOL Multiphysics was utilized to solve the time-dependent heat transport Equation (1) in a 2D axisymmetric domain (Figure 1) using the finite element method. A mapped mesh is used for domain discretization with a minimum mesh size of 1 nm along z and 25 nm along r. The simulations were performed for a single laser pulse, since there is no thermal effect of one pulse on the next pulse, due to a long time between laser pulses (pulse repetition frequency 10Hz). A transient analysis was thus done with time scale varying from 0 ns to 200 ns and variable time steps selected from 0.2 to 10 ns using the implicit backward differentiation formula (BDF) method. The resulting linear system of equations was solved using the PARDISO solver. The materials thermophysical properties were expressed as a function of temperature to reflect more realistic physical phenomena. Since the ns-laser beam wavelength used is 248 nm, the materials optical properties corresponding to 248 nm were used for simulating the temperature distribution across the multilayer stack. The full list of parameters used in the simulations is given in Tables S1 and S2 of the Supporting Information.

3. Results and Discussion

In order to determine the optimal laser fluence for the crystallization of ZrO_2 in the as-grown films, a knowledge of the temperature distribution and temporal evolution across the multilayer structure is essential.[30] Thus, the heating and cooling rates need to be calculated during the process, and the right electrode materials used to give optimum heat conduction and generation of

© 2023 The Authors. Advanced Science published by Wiley-VCH GmbH

21983844, 2023, 15, Downloaded from https://onlinelibrary.wiley.com/doi/10.1002/advs.202207390 by Cochrane Portugal, Wiley Online Library on [26/07/2023]. See the Terms and Conditions (https://onlinelibrary.wiley.com/terms-and-conditions) on Wiley Online Library for rules of use; OA articles are governed by the applicable Creative Commons License

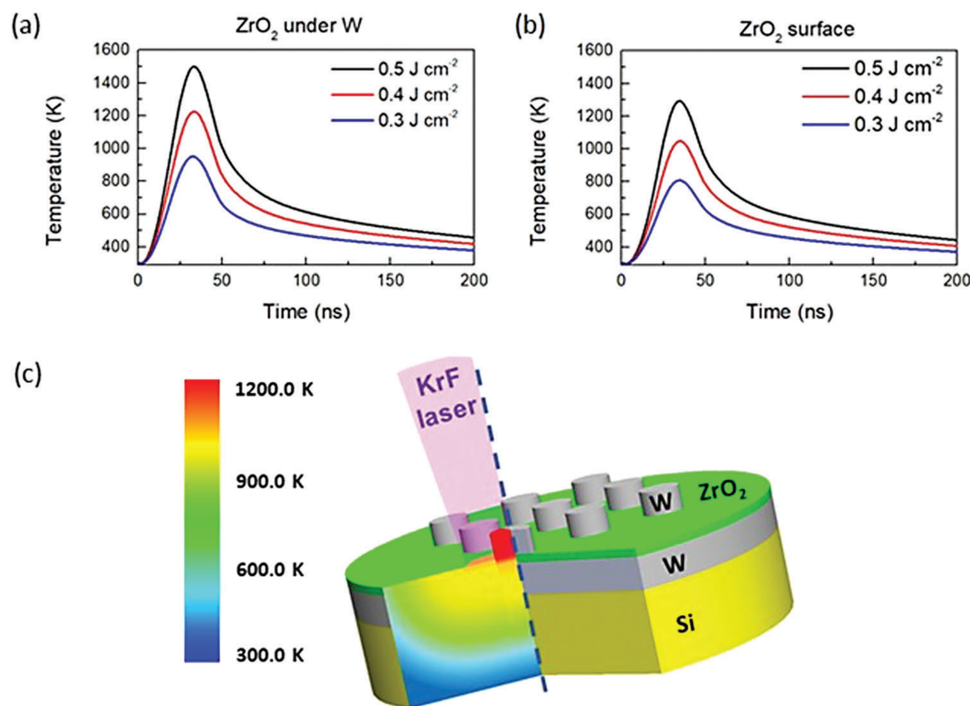

Figure 2. Simulated temperature distribution as a function of time for the NLA process with a fluence of 0.4 Jcm^{-2} for a) ZrO_2 surface under the W top electrode (P1 in Figure 1) and b) uncovered ZrO_2 surface (P2 in Figure 1). c) Schematic representation of the structure on the right side and in-depth temperature gradient distribution across the layers. The dashed blue line separates both sides.

thermal strain in the oxide film necessary for stabilization of the ferroelectric phase. In this regard, W is a good choice because of its high thermal conductivity and the aforementioned TEC value. **Figure 2**a,b shows the temperature profile as a function of time for different laser fluences on the ZrO_2 surface under a top W electrode, compared to a ZrO_2 surface with no electrode. It is observed that the temperature reached in the ZrO_2 layer under the top W electrode (P1 in Figure 1) is higher than that in the ZrO_2 surface exposed directly to the laser beam (P2 in Figure 1), irrespective of the laser fluence used. This is due to the higher heat absorption by the *W* layer upon laser incidence, when compared to the uncoated ZrO_2, allowing it to reach higher temperatures. For the absorption length of *W* (see Table S2, Supporting Information), ≈98% of laser energy (not reflected) will be absorbed in the capping *W*, leading to a significative heating of the top W electrode. Due to the large absorption length for ZrO_2 (≈128 nm) almost no laser energy is absorbed in the ZrO_2 film. This means that only ≈2% of laser energy transmitted through the top electrode will reach the bottom *W* electrode. In the case of laser incidence directly in ZrO_2 film, the bottom electrode gets heated, since almost all laser energy transmitted will reach it. Therefore, the lower temperature of the uncovered ZrO_2 film upon laser incidence, compared to the W-electrode-covered-ZrO_2 layer is explained by the contribution of radiative heat losses, resulting in a lower net heat absorption in this layer.

Typically, the *o*-phase in ZrO_2 films is achieved after a rapid-thermal annealing (RTA) at a temperature equal to or higher than 600 °C.[30,31] From our simulations was predicted that a minimum laser fluence of 0.4 J cm^{-2} should be used in the NLA process in order to crystallize the ZrO_2 layer. Figure 2c shows on the right side of the blue dashed line a schematic representation of the structure, while the left side shows the simulated in-depth temperature profile across the structure, 30 ns after laser incidence, for a NLA process with a laser fluence of 0.4 J cm^{-2}. The largest temperature difference in Figure 2c occurs in the Si substrate, ≈600 K, while the temperature difference is only 100K in the ZrO_2 thin film. The high temperatures, above 900 K, in the ZrO_2 layer, not only allow the kinetic barrier for the tetra-ortho phase transition to be overcome but also lead to the stabilization of the *o*-phase due to the high tensile thermal stresses induced by the large difference in TEC of W and ZrO_2 layers. The top W layer, thus plays a fundamental role in the NLA process of the ZrO_2 film, working not only as a capping protection layer from laser energy pulse, but also contributing to the heating of ZrO_2 layer and generating the tensile thermal stresses necessary for stabilization of the *o*-phase.

After performing the NLA with a fluence of 0.4 J cm^{-2}, the samples were structurally characterized by X-ray diffraction (XRD). **Figure 3** shows the XRD pattern for the $Si/SiO_x/W/ZrO_2$ and $Si/SiO_x/W/ZrO_2/W$ structures after the NLA. One significant diffraction peak centered at $2\theta = 30.45°$ ($d = 2.93$ Å) is observed in both structures. No other peaks were observed, indicating no significant WO_x formation.

The 30.45° diffraction peak could be attributed to the presence of the cubic (*c*)-phase (111), *o*-phase (111), tetragonal (*t*)-phase (101), or the *r*-phase (111) planes.[32,24] The *c*-phase and *t*-phase nanoscale ZrO_2 are known for their paraelectric and antiferroelectric characteristics, respectively.[33] Owing to the limitation of the XRD technique, it is not possible to unequivocally distinguish between the ferroelectric *o*-phase or *r*-phases and other

 © 2023 The Authors. Advanced Science published by Wiley-VCH GmbH

21983844, 2023, 15, Downloaded from https://onlinelibrary.wiley.com/doi/10.1002/advs.202207390 by Cochrane Portugal, Wiley Online Library on [26/07/2023]. See the Terms and Conditions (https://onlinelibrary.wiley.com/terms-and-conditions) on Wiley Online Library for rules of use; OA articles are governed by the applicable Creative Commons License

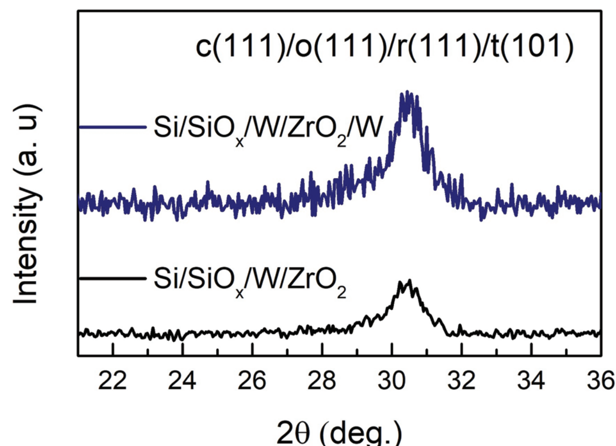

Figure 3. XRD pattern of the Si/SiOx/W/ZrO_2 and Si/SiOx/W/ZrO_2/W structures.

nonferroelectric phases. Moreover, the XRD patterns reveal that no significant differences are observed in the XRD peak when comparing both samples. In addition, the samples were amorphous before any NLA process.

We also used electron backscatter diffraction (EBSD) and transmission electron microscopy to clearly identify the phases present in the ZrO_2 films without and with the top W layer, respectively. In the case of EBSD measurements beneath the W layer is not possible. For EBSD, 15,000 election backscatter patterns were collected across an ≈1 mm area of the film. Electron backscatter diffraction patterns (EBSPs) were indexed using 12 bands and a Hough resolution of 70. A polycrystalline structure was identified, though the low-resolution of EBSPs collected prevented indexing for ≈75% of patterns. The small film thickness precluded collection of high-resolution EBSP despite exposure times of up to 500 ms. Additionally, it is not possible to index patterns where grains were smaller than the electron interaction volume (<10 nm). Another consideration, given the low pattern resolution, is the effect of pseudosymmetry and mis-indexing of orthorhombic and tetragonal phases. For low-resolution patterns, it can be challenging to distinguish between some orientations of *o*-phase and *t*-phase. Despite the aforementioned challenges, the presence of *o*-, *m*-, and *t*- phases was confirmed from higher-quality patterns, for example, those in **Figure 4** (a,b, and c for *o*-, *m*-, and *t*- phases respectively). For these three EBSPs, 9 bands were matched for the *t*- and *m*-phase patterns, and 10 bands for the *o*-phase. The indexed patterns have a mean angular deviation (MAD) of 0.60°, 0.68°, and 0.58° respectively for *o*-, *m*-, and *t*-phases. Mean angular deviation (MAD) is defined as the angular deviation between the observed and simulated lattice plane orientations. A value below 1° is typically acceptable for phase identification, but in the case of pseudo-symmetric phases, it has been found that MAD values <0.7° significantly reduce the rate of mis-indexing.[34]

Given the high number of nonindexed patterns and the potential for mis-indexing, an absolution phase ratio cannot be obtained. However, of the patterns indexed the most common fitting is the *o*-phase (≈65%) and the *o*- patterns have the average mean MAD value (0.9°) which supports the identification of *o*- as the mostly likely primary phase. Additionally, of the *o*- indexed regions, a texturing is demonstrated, with the [111] neat surface normal (See Figure S1, Supporting Information).

Figure 5a shows a large-area HRTEM image exhibiting the W/ZrO_2/W layers deposited on top of the Si substrate with a native SiO_x layer of 2–3 nm. The thickness of the ZrO_2 layer is 8 ± 1 nm, while the bottom W layer thickness is 14 ± 1 nm. Moreover, the interfaces between the substrate and the W layer and also between the W layers and the ZrO_2 layer are clean with no visible discontinuity.

The fully crystallized state and texturing of the ZrO_2 layer can be observed on the large-area HRTEM image showing $(111)_{ZrO2}$ lattice fringes with a preferential orientation parallel to the substrate. The film texturing is better illustrated by the Fourier-filtered image in Figure 5b. The $(111)_{ZrO2}$ texturing of the ZrO_2 thin film is demonstrated on one side by the power spectrum (inserted in Figure 5b), showing the strong $(111)_{ZrO2}$ spots aligned along a direction perpendicular to the substrate. On the other hand, we mapped the spatial distribution of the $(111)_{ZrO2}$ lattice fringes in the HRTEM micrograph by selecting the $(111)_{ZrO2}$ peak in the associated whole-frame power spectrum. The filtered HRTEM image shows that the $(111)_{ZrO2}$ lattice fringes are visible and aligned (approximately) parallel to the substrate across the whole HRTEM micrograph, thus validating the ZrO_2 film texturing.

In order to analyze the crystalline phase in the ZrO_2 film, we examined the Fast Fourier Transform (FFT) of the HRTEM image of a zone axis-oriented ZrO_2 grain selected from the thinner part of the specimen (Figure 5c,d). The *o*-phase can be reliably discerned from the monoclinic phase by analyzing the {111} diffraction peaks: the (111)o peak corresponds to an interplanar distance of 0.3 nm between the equivalent {111} planes, while in the case of the monoclinic phase the (111)m peak splits in two, corresponding to the {111}m and {11-1}m families of planes, spaced at 0.286 nm and 0.322 nm, respectively. In our case, from the measurements performed both on the HRTEM micrograph and on the FFT picture performed on an area which contains an oriented ZrO_2 crystallite (Figure 5b), we obtained the following interplanar distances: 0.296 nm + −0.004 nm, which can be assigned to {111} planes of the *o*-phase with space group $Pca2_1$,[35] but this measured distance can be assigned also to the {101} family of planes of the tetragonal phase with space group $P4_2/nmc$. The (101) planes of the tetragonal phase are spaced at a 0.3006 nm distance, which is within the error limits of our measurements. Since the FFT pattern, shown in Figure 5d, contains a well-defined pattern of spots, thus proving a high crystallization degree in terms of grain size and preferential crystallographic orientation, we measured and assigned three peaks to the (1-1-1), (111), and (200) planes of the *o*-structure of ZrO_2 the crystallite being viewed along the [01-1] zone axis. The structure parameters for this spatial group are: $a = 0.52336$ nm, $b = 0.52684$ nm, and $c = 0.54184$ nm. Figure 5d shows a magnified view of a ZrO_2 crystallite, which contains the atomic structural model of the orthorhombic structure embedded to emphasize the correct interpretation of the experimental results.

The HRTEM measurements performed on the ZrO_2 crystallite below the top W layer confirm the textured growth with a preferential orientation of the {111} family of planes. For the direction along the normal surface, bearing in mind the indexation used in the FFT pattern from Figure 5b, the [1-1-1] direction makes an

 © 2023 The Authors. Advanced Science published by Wiley-VCH GmbH

21983844, 2023, 15, Downloaded from https://onlinelibrary.wiley.com/doi/10.1002/advs.202207390 by Cochrane Portugal, Wiley Online Library on [26/07/2023]. See the Terms and Conditions (https://onlinelibrary.wiley.com/terms-and-conditions) on Wiley Online Library for rules of use; OA articles are governed by the applicable Creative Commons License

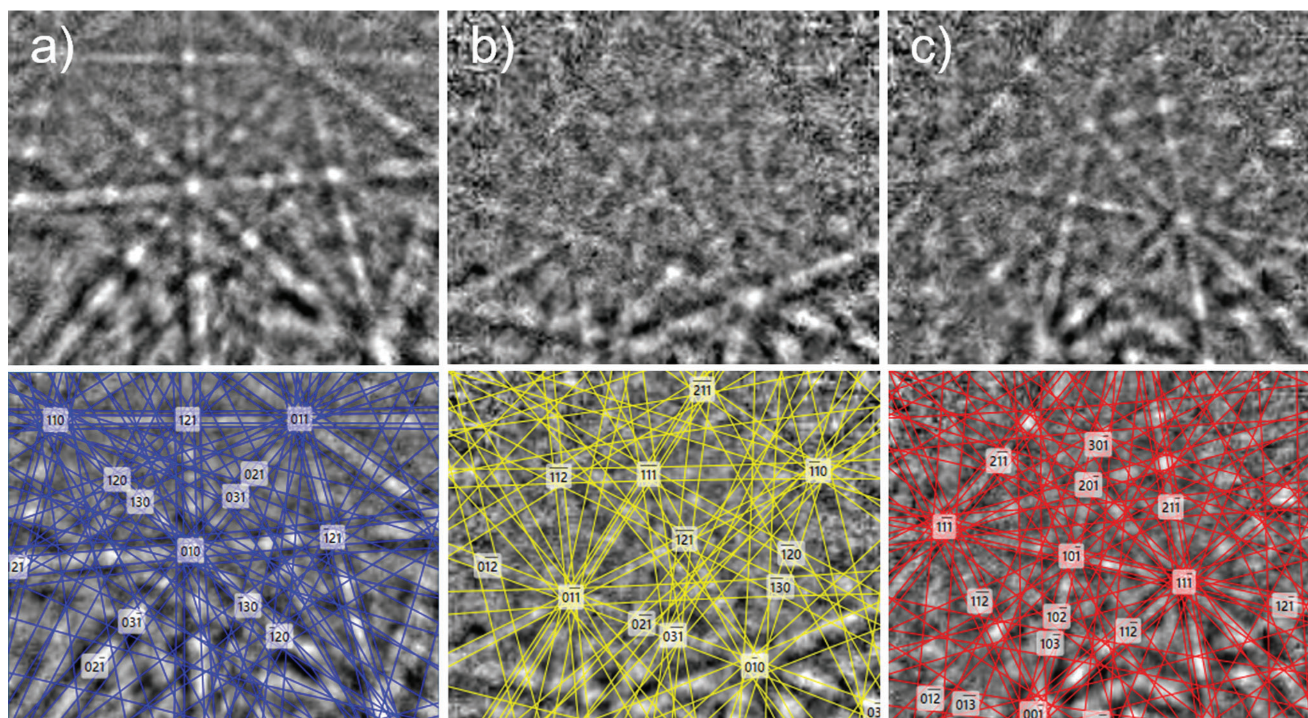

Figure 4. Example of electron backscatter diffraction patterns (top) and corresponding fits (bottom) for a) orthorhombic phase fit with 10 bands and MAD of 0.60°, b) monoclinic phase fit with 9 bands and MAD of 0.68°, and c) tetragonal phase fit with 9 bands and MAD of 0.58°.

angle of ≈5° with the surface normal, whereas, for the other direction, in-plane, the [111] direction makes an angle of ≈12° with the direction perpendicular to the normal surface, as presented in Figure S3, Supporting Information. Therefore, the ZrO_2 is textured with the [111] direction almost parallel to the surface normal, similar to what was observed from EBSD results performed on the ZrO_2 film without the W top layer.

In Figure 5f, we simulate using VESTA software the atomic structural model of ZrO_2 along the [01-1] zone axis and we also determined the distances between the (1-1-1) and (111) set of planes. It can be observed that there is a perfect agreement between the simulated structure and the experimental data provided by the HRTEM pictures. In order to be able to confirm the crystalline structure of the ZrO_2 crystallite, we simulated HRTEM patterns and atomic structural models, using the multislice technique, with the use of the *x*HREM software kit. In each case, a series of simulated images were generated according to the sample thickness and the defocus of the objective lens, as it is displayed in Figure S4, Supporting Information. The intensity modulation of HRTEM images was investigated and associated with the atomic structure by simulating the HRTEM patterns with the multislice technique. A matrix of HRTEM patterns was simulated along the zone axis in which the ZrO_2 crystallite is oriented: B = [01-1] for the orthorhombic structure of ZrO_2. Moreover, in order to confirm the correct interpretation of the experimental data, the HRTEM simulated image was overlapped with the experimental HRTEM image, as shown in Figure 5e. It is possible to observe a good agreement between the experimental pattern and the one simulated for a defocus of −10 nm and a thickness of 40 nm and therefore we were able to further confirm the presence of the *o*-phase in the ZrO_2 film.

The HRTEM images in **Figure 6** refer to the microstructural characterization of the W bottom and top layers. Due to the low sputtering rate of W during the Ar+ ion milling and the shadowing effect played by the hard W layers, we could not identify a location where both layers were simultaneously thin enough for HRTEM imaging. Therefore, the HRTEM analyses of the top and bottom W layers were performed in two different locations where either the top or the bottom W layer had the right thickness for HRTEM imaging. Figure 6a,b,c,d are large-area and enlarged HRTEM images of the bottom and top W layers, respectively. The enlarged HRTEM images in Figure 6b,d contain the FFT pattern performed on the square areas marked in Figure 6a,c. By analyzing the FFT patterns we could identify the cubic crystalline structure of metallic W (space group Im-3m, a = 0.31648 nm) as a unique phase inside both the bottom and top layers. At this level, by using this technique, no WO_x structure could be identified, thus confirming the XRD results where no trace of WO_x phase is identified.

We observed that with a fluence of 0.5Jcm^{-2}, the surface of the ZrO_2 layer (without a top W layer) became damaged, as shown in the Figure S2, Supporting Information. However, with a fluence of 0.4 J cm^{-2} we do not observe a significant damage of the layers, as can be seen in the HRTEM images. In addition, the temperature difference predicted by the simulation in the ZrO_2 layer, as discussed before, shouldn´t have any significant effect on the uniformity of the ZrO_2 crystallization process, as can be observed in the HRTEM analysis from Figure 5.

Figure 7a shows the room temperature pristine polarization-electric field (P–E) hysteresis loops of the W/ZrO_2/W film capacitor. A well-saturated hysteresis loop was obtained, which confirms the ferroelectric nature of the ZrO_2 film. To further

© 2023 The Authors. Advanced Science published by Wiley-VCH GmbH

21983844, 2023, 15, Downloaded from https://onlinelibrary.wiley.com/doi/10.1002/advs.202207390 by Cochrane Portugal, Wiley Online Library on [26/07/2023]. See the Terms and Conditions (https://onlinelibrary.wiley.com/terms-and-conditions) on Wiley Online Library for rules of use; OA articles are governed by the applicable Creative Commons License

21983844, 2023, 15, Downloaded from https://onlinelibrary.wiley.com/doi/10.1002/advs.202207390 by Cochrane Portugal, Wiley Online Library on [26/07/2023]. See the Terms and Conditions (https://onlinelibrary.wiley.com/terms-and-conditions) on Wiley Online Library for rules of use; OA articles are governed by the applicable Creative Commons License

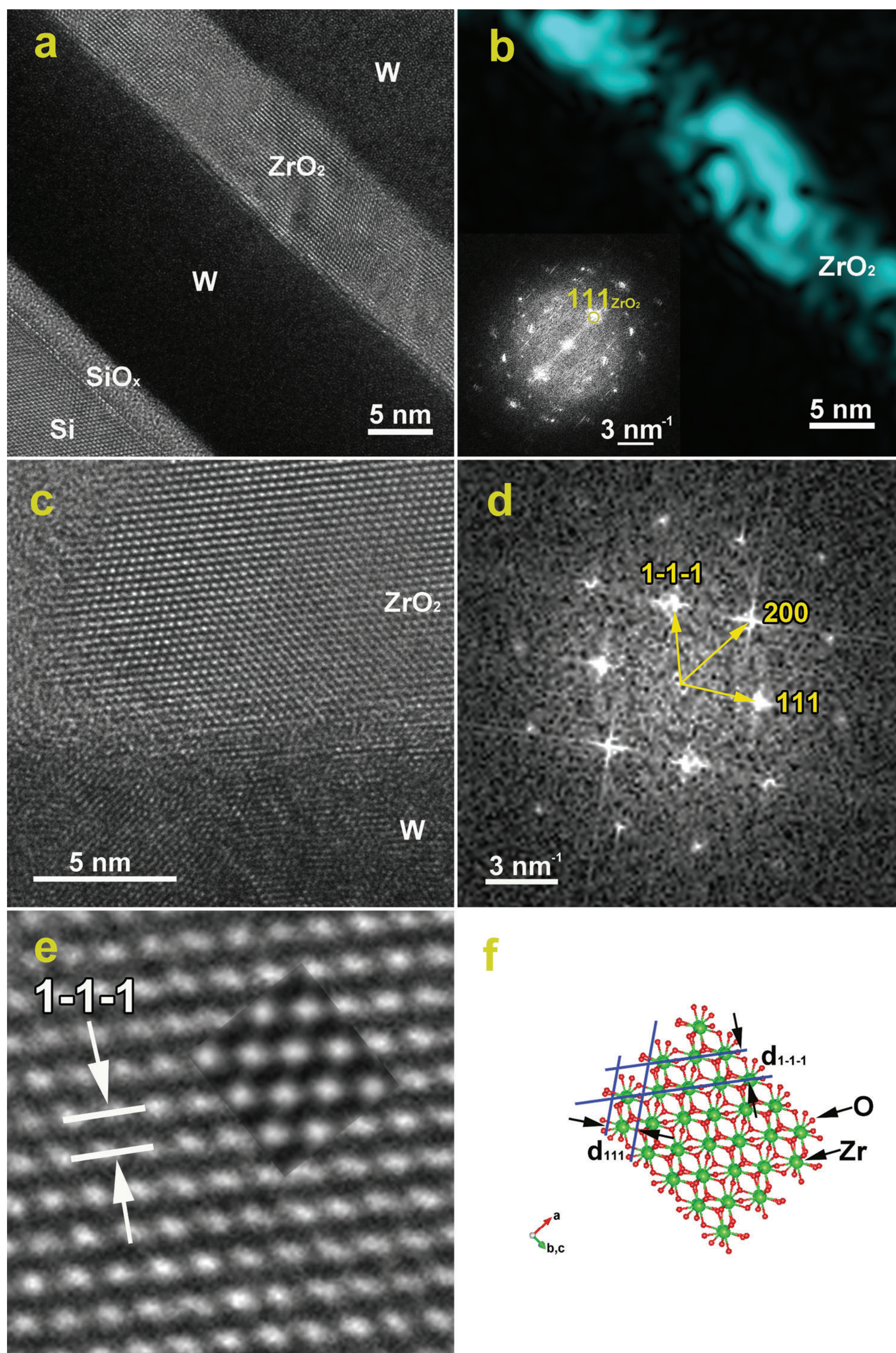

Figure 5. a) Large-area HRTEM image of the Si/SiO_x/W/ZrO_2/W structure; b) Spatial distribution of the $(111)_{ZrO2}$ lattice fringes obtained by filtering the power spectrum (inserted) of the HRTEM micrograph in (a); c) HRTEM image of a zone axis oriented ZrO_2 grain at the W/ZrO_2 interface. d) FFT pattern from an area containing the ZrO_2 crystallite in (c); e) enlarged HRTEM image of the ZrO_2 crystallite in (c) and the embedded simulated HRTEM pattern of the orthorhombic ZrO_2 (defocus -10 nm, thickness 40 nm); f) Atomic structural model of ZrO_2 in the [01-1] orientation in perfect agreement with structural data provided by the experimental images.

© 2023 The Authors. Advanced Science published by Wiley-VCH GmbH

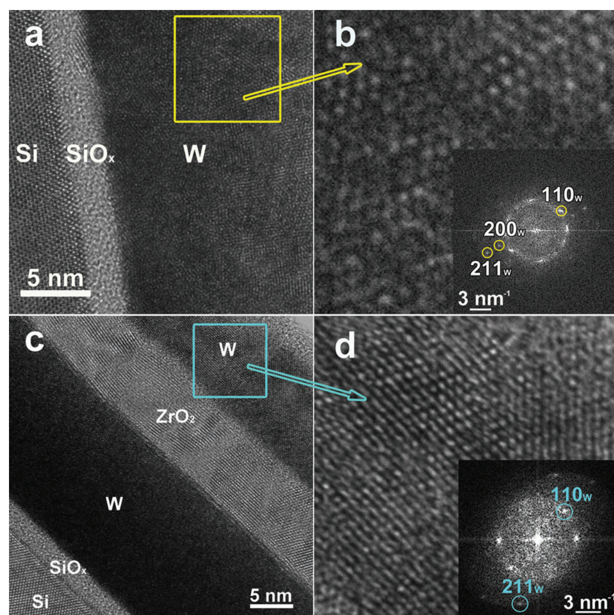

Figure 6. a). HRTEM image of the $Si/SiO_x/W$ structure and b) magnified image of the lattice fringes of W structure and the FFT pattern embedded in the HRTEM picture, performed on an area marked by the yellow square in (a), in which we indexed and assigned two peaks for the cubic structure of the bottom W structure, c) HRTEM image of the $Si/SiO_x/W/ZrO_2/W$ structure and d) magnified image of the lattice fringes of W structure together with the FFT pattern of the area marked by the blue square in (c).

confirm the ferroelectric nature of the films, frequency-dependent P-E hysteresis loops are shown in Figure S5, Supporting Information. With increasing frequency, there is a slight decrease of P_r and P_s, while E_c increases. A similar behavior was observed in HZO films.[36] The average values of P_s, P_r and E_c for the $W/ZrO_2/W$ film capacitor are 12.8 µC cm^{-2}, 12.7 µC cm^{-2} and 1.2 MV cm^{-1}, respectively. ZrO_2 films annealed by rapid thermal annealing (RTA) reveal the formation of a WO_3 layer with a 1–2 nm thickness. This layer forms when W electrodes scavenge oxygen during annealing, leaving the ZrO_2 oxygen deficient.[37] The existence of this WO_3 layer leads to the observation of a pronounced imprint effect. In addition, the NLA sample revealed a lower E_c and a higher P_r, which are both crucial for low-power memory applications. **Table 1** shows a comparison between the average values of P_s, P_r and E_c for the $W/ZrO_2/W$ film capacitor

Table 1. Comparison of the thickness, P_s, P_r and E_c values for different capacitors based on ZrO_2 thin films.

Structure	Thickness (nm)	P_r [µC cm^{-2}]	P_s [µC cm^{-2}]	E_c [MV cm^{-1}]	Ref.
$Pt/ZrO_2/Pt$	6.5	≈50	≈57	4.6	[22]
$Nb:STO/ZrO_2/Au$	8	10.8	10.8	1.5	[30]
$Si/SiO_2/ZrO_2/TiN$	10	≈13	≈22	-	[38]
$TiN/ZrO_2/TiN$	45	7	≈10	≈1	[39]
$Ge/ZrO_2/Al$	17	6	≈13	1.5	[40]
$Pt/ZrO_2/Pt$	100	≈12	≈22	≈1	[41]
$Pt/ZrO_2/Pt$	19.6	≈12	≈12	≈2.0	[31]
$Pt/ZrO_2/Au$	5	21	44	1.6	[24]
$Pt/ZrO_2/Pt$	7.5	≈6.4	≈6.4	≈1.5	[33]
$W/ZrO_2/W$	8	12.7	12.8	1.2	This work

obtained in this work with the ones presented in the recent literature based on ZrO_2 thin films capacitors. The high P_r and P_s values together with low E_c confirm that the present capacitors are promising for future nonvolatile memory. As observed from Table 1, there are no reports on sub-10 nm thick ferroelectric ZrO_2 films with P_r higher than 10 µC cm^{-2} and a E_c below 1.5 MV cm^{-1}. In order to further elucidate this, we have plotted the P_r as a function of E_c, Figure 7b. With the aim of achieving low-power memory devices, it is possible to observe that there is only a previous report of a film with a similar P_r but with lower E_c, than the values reported in this work, and the film was 12.5 times thicker than in this work. Therefore, the present capacitors exhibit a high P_r and a low E_c, which is crucial for memory devices.

Figure 7c shows the evolution of both $+P_r$ and $-P_r$ as a function of the number of cycles. It is possible to observe a slight increase of the $|+P_r|$ and $|-P_r|$ from ≈12.7 µC cm^{-2} up to ≈17 µC cm^{-2} after 1.8×10^5 cycles. This increase in Pr of 4.3 µC cm^{-2} is attributed to the so-called wake-up effect. This wake-up effect is ascribed to the migration of point defects (mainly oxygen vacancies) and/or a transition from nonferroelectric (*m*- and *t*-phase) to the ferroelectric phase (especially at the interfacial region).[2] After this, both $+P_r$ and $-P_r$ values remain stable up to 6.0×10^5 cycles, confirming the good endurance of the devices.

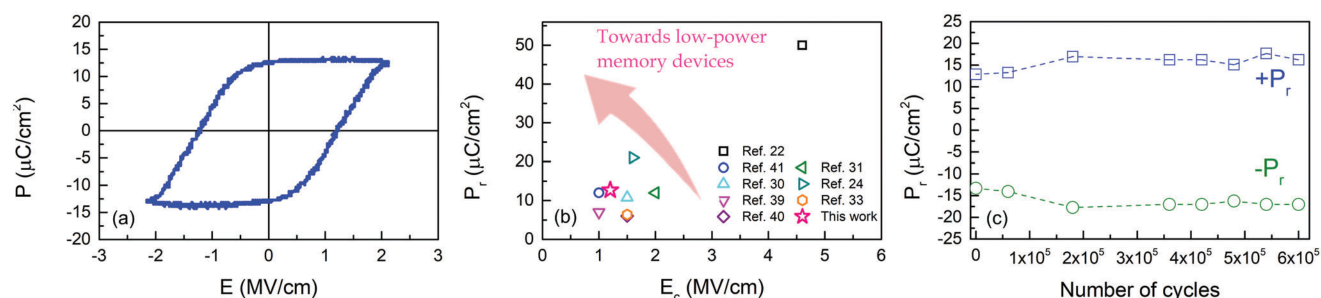

Figure 7. a). Polarization (*P*)-electric field (*E*) hysteresis loop for the $W/ZrO_2/W$ film capacitor. b) Remanent polarization, P_r, as a function of the coercive field, E_c for different capacitors based on ZrO_2 thin films. The arrows show the aimed direction for device improvement. c) P_r as a function of the number of field switching cycles for $W/ZrO_2/W$ thin film capacitor.

 © 2023 The Authors. Advanced Science published by Wiley-VCH GmbH

21983844, 2023, 15, Downloaded from https://onlinelibrary.wiley.com/doi/10.1002/advs.202207390 by Cochrane Portugal, Wiley Online Library on [26/07/2023]. See the Terms and Conditions (https://onlinelibrary.wiley.com/terms-and-conditions) on Wiley Online Library for rules of use; OA articles are governed by the applicable Creative Commons License

4. Conclusions

In this work, we have demonstrated the effectiveness of nanosecond laser annealing of amorphous ZrO_2 films with W electrodes, for creating crystalline ferroelectric ZrO_2 films. The optimum conditions of the rapid laser annealing were guided by COMSOL Multiphysics simulations of laser heating of the multilayer stack. Using XRD, EBSD, and TEM analyses, the formation of an orthorhombic phase of ZrO_2 was confirmed as the ferroelectric phase in the films. The films showed a spontaneous polarization of ≈12.8 μC cm^{-2}, a remnant polarization of 12.7 μC cm^{-2}, a coercive field of 1.2 MV cm^{-1}, and a polarization retention of 6.0 × 10^5 cycles. A small wake-up effect was also observed, attributed to the migration of point defects such as oxygen vacancies, and/or a transition from nonferroelectric (*m*- and *t*-phase) to the ferroelectric *o*-phase. Overall, this study shows the strong potential for the fabrication of ferroelectric ZrO_2 thin films by a nanosecond laser annealing process from amorphous precursor films. Such films have strong promise for the next generation of memory and sensing devices.

Supporting Information

Supporting Information is available from the Wiley Online Library or from the author.

Acknowledgements

A.P.S.C. and M.C.I. contributed equally to this work. This work was supported by the Portuguese Foundation for Science and Technology (FCT) in the framework of the Strategic Funding Contract UIDB/04650/2020. This work has received funding from the European Union's Horizon 2020 research and innovation program under grant agreement No 958174 (M-ERA-NET3/0003/2021—NanOx4EStor). M. C. I. and C. G. acknowledge the financial support by a grant of the Ministry of Research, Innovation and Digitization, CNCS/CCCDI – UEFISCDI, project number COFUND-M-ERANET-3-NanOx4Estor, within PNCDI III and POC 332/390008/29.12.2020-SMIS 109522. The authors acknowledge the CERIC-ERIC Consortium for access to experimental facilities and financial support under proposals 20202037, 20202038, and 20192055. The authors would also like to thank José Santos for technical support in the Thin Film Laboratory at CF-UM-UP. J.L.M-D. thanks the ERC grant, EU-H2020-ERC-ADG # 882929, EROS. And the Royal Academy of Engineering, grant CIET1819_24. MOH thanks the Herchel Smith foundation of Cambridge for a research fellowship. This work made use of the University of Cambridge Wolfson Electron Microscopy Suite.

Conflict of Interest

The authors declare no conflict of interest.

Data Availability Statement

The data that support the findings of this study are available from the corresponding author upon reasonable request.

Keywords

binary oxides, ferroelectricity, nanosecond laser annealing, orthorhombic phase

Received: December 15, 2022
Revised: February 22, 2023
Published online: March 22, 2023

[1] U. Schroeder, M. H. Park, T. Mikolajick, C. S. Hwang, *Nat. Rev. Mater.* **2022**, *7*, 653.
[2] J. P. B. Silva, K. C. Sekhar, R. F. Negrea, J. L. MacManus-Driscoll, L. Pintilie, *Appl. Mater. Today* **2022**, *26*, 101394.
[3] T. S. Böscke, J. Müller, D. Bräuhaus, U. Schröder, U. Böttger, J. Sundqvist, P. Kücher, T. Mikolajick, L. Frey, *Appl. Phys. Lett.* **2011**, *99*, 102903.
[4] J. Hou, W. Jiang, Y. Fang, Y. Wang, X. Yin, F. Huang, *ECS J. Solid State Sci. Technol.* **2012**, *1*, R57
[5] S. Mueller, J. Mueller, A. Singh, S. Riedel, J. Sundqvist, U. Schroeder, T. Mikolajick, *Adv. Funct. Mater.* **2012**, *22*, 2412.
[6] T. Song, H. Tan, N. Dix, R. Moalla, J. Lyu, G. Saint-Girons, R. Bachelet, F. Sánchez, I. Fina, *ACS Appl. Electron. Mater.* **2021**, *3*, 2106
[7] Y. Yun, P. Buragohain, M. Li, Z. Ahmadi, Y. Zhang, X. Li, H. Wang, J. Li, P. Lu, L. Tao, H. Wang, Jeffrey E. Shield, E. Y. Tsymbal, A. Gruverman, X. Xu, *Nat. Mater.* **2022**, *21*, 903.
[8] J. Müller, T. S. Böscke, U. Schröder, S. Mueller, D. Bräuhaus, U. Böttger, L. Frey, T. Mikolajick, *Nano Lett.* **2012**, *12*, 4318.
[9] J. P. B. Silva, K. C. Sekhar, H. Pan, J. L. MacManus-Driscoll, M. Pereira, *ACS Energy Lett.* **2021**, *6*, 2208.
[10] B. Liu, Y. Cao, W. Zhang, Y. Li, *Appl. Phys. Lett.* **2021**, *119*, 172902.
[11] S. Estandía, N. Dix, J. Gazquez, I. Fina, J. Lyu, M. F. Chisholm, J. Fontcuberta, F. Sánchez, *ACS Appl. Electron. Mater.* **2019**, *1*, 1449.
[12] S. Estandía, J. Gàzquez, M. Varela, N. Dix, M. Qian, R. Solanas, I. Fina, F. Sánchez, *J. Mater. Chem.* **2021**, *9*, 3486.
[13] S. S. Fields, T. Cai, S. T. Jaszewski, A. Salanova, T. Mimura, H. H. Heinrich, M. D. Henry, K. P. Kelley, B. W. Sheldon, J. F. Ihlef, *Adv. Electron. Mater.* **2022**, *8*, 2200601.
[14] T. Song, H. Tan, A. C. Robert, S. Estandia, J. Gazquez, F. Sanchez, I. Fina, *App. Mater. Today* **2022**, *29*, 101621.
[15] D. Wang, Y. Zhang, J. Wang, C. Luo, M. Li, W. Shuai, R. Tao, Z. Fan, D. Chen, M. Zeng, J. Y. Dai, X. B. Lu, J. M. Liu, *J. Mater. Sci. Technol.* **2022**, *104*, 1.
[16] Y. Goh, S. H. Cho, S. H. Ko Park, S. Jeon, *Nanoscale* **2022**, *12*, 9024.
[17] J. Bouaziz, P. R. Romeo, N. Baboux, B. Vilquin, *ACS Appl. Electron. Mater.* **2019**, *1*, 1740.
[18] Z. Zhang, S. L. Hsu, V. A. Stoica, H. Paik, E. Parsonnet, A. Qualls, J. Wang, L. Xie, M. Kumari, S. Das, Z. Leng, M. McBriarty, R. Proksch, A. Gruverman, D. G. Schlom, L. Q. Chen, S. Salahuddin, L. W. Martin, R. Ramesh, *Adv. Mater.* **2021**, *33*, 2006089.
[19] R. Cao, Y. Wang, S. Zhao, Y. Yang, X. Zhao, W. Wang, X. Zhang, H. Lv, Q. Liu, M. Liu, *IEEE Electron. Device Lett.* **2018**, *39*, 1207.
[20] A. Kashir, H. Kim, S. Oh, H. Hwang, *ACS Appl. Electron. Mater.* **2021**, *3*, 629.
[21] V. Lenzi, J. P. B. Silva, B. Šmíd, V. Matolín, C. M. Istrate, C. Ghica, J. L. MacManus-Driscoll, L. Marques, *Energy Environ. Mater.* **2022**, *0*, 2575.
[22] K. W. Huang, S. H. Yi, Y. S. Jiang, W. C. Kao, Y. T. Yin, D. Beck, V. Korolkov, R. Proksch, J. Shieh, M. J. Chen, *Acta Mater.* **2021**, *205*, 116536.
[23] J. P. B. Silva, R. F. Negrea, M. C. Istrate, S. Dutta, H. Aramberri, J. In´ĩguez, F. G. Figueiras, C. Ghica, K. C. Sekhar, A. L. Kholkin, *ACS Appl. Mater. Interfaces* **2021**, *13*, 51383.
[24] J. P. B. Silva, K. C. Sekhar, R. F. Negrea, C. Ghica, D. Dastan, M. J. M. Gomes, *Ceram. Int.* **2022**, *48*, 6131.
[25] S. S Cheema, N. Shanker, S. L. Hsu, Y. Rho, C. H. Hsu, V. A. Stoica, Z. Zhang, J. W Freeland, P. Shafer, C. P. Grigoropoulos, J. Ciston, S. Alahuddin, *Science* **2022**, *6*, 648.

 © 2023 The Authors. Advanced Science published by Wiley-VCH GmbH

21983844, 2023, 15, Downloaded from https://onlinelibrary.wiley.com/doi/10.1002/advs.202207390 by Cochrane Portugal, Wiley Online Library on [26/07/2023]. See the Terms and Conditions (https://onlinelibrary.wiley.com/terms-and-conditions) on Wiley Online Library for rules of use; OA articles are governed by the applicable Creative Commons License

[26] R. P. Haggerty, P. Sarin, Z. D. Apostolov, P. E. Driemeyer, W. M. Kriven, *J. Am. Ceram. Soc.* **2014**, *97*, 2213.
[27] T. Schenk, C. M. Fancher, M. H. Park, C. Richter, C. Künneth, A. Kersch, J. L. Jones, T. Mikolajick, U. Schroeder, *Adv. Electron. Mater.* **2019**, *5*, 1900303.
[28] N. Volodina, A. Dmitriyeva, A Chouprik, E Gatskevich, A Zenkevich, *Phys. Status Solidi Rapid. Res. Lett.* **2021**, *15*, 2100082.
[29] T. Ali, R. Olivo, S. Kerdilès, D. Lehninger, M. Lederer, D. Sourav, A-S. Royet, A. Sünbül, A. Prabhu, K. Kühnel, M. Czernohorsky, M. Rudolph, R. Hoffmann, C. Charpin-Nicolle, L. Grenouillet, T. Kämpfe, K. Seidel, *2022 IEEE International Memory Workshop, IMW 2022 – Proceedings*, Institute of Electrical and Electronics Engineers Inc. , Dresden, Germany **2022**.
[30] L. Grenouillet, T. Francois, J. Coignus, S. Kerdilès, N. Vaxelaire, C. Carabasse, F. Mehmood, S. Chevalliez, C. Pellissier, F. Triozon, F. Mazen, G. Rodriguez, T. Magis, V. Havel, S. Slesazeck, F. Gaillard, U. Schroeder, T. Mikolajick, E. Nowak, *2020 IEEE Symposium on VLSI Technology*, Honolulu, HI, USA, **2020**, pp. 1–2, https://doi.org/10.1109/VLSITechnology18217.2020.9265061.
[31] B. T. Lin, Y. W. Lu, J. Shieh, M. J. Chen, *J. Eur. Ceram. Soc.* **2017**, *37*, 1135.
[32] M. Materano, P. Reinig, A. Kersch, M. Popov, M. Deluca, T. Mikolajick, U. Boettger, U. Schroeder, *Phys. Status Solidi RRL* **2022**, *16*, 2100589.
[33] C. Y. Wang, C. I. Wang, S. H. Yi, T. J. Chang, C. Y. Chou, Y. T. Yin, M. Shiojiri, M. J. Chen, *Mater. Des.* **2020**, *195*, 109020.
[34] T. Nagaya, S. R. Wallis, Y. S. Akira, M. k. Yusuke, S. S. Uehara, M. Matsumoto, *J. Struct. Geo.* **2017**, *95*, 127.
[35] https://next-gen.materialsproject.org/materials/mp-556605?formula=ZrO2.
[36] Y. Li, J. Li, R. Liang, R. Zhao, B. Xiong, H. Liu, H. Tian, Y. Yang, T.-L. Ren, *Appl. Phys. Lett.* **2019**, *114*, 142902.
[37] R. M. P. Pereira, M. C. Istrate, F. G. Figueiras, V. Lenzi, B. M. Silva, M. Benamara, K. N. Romanyuk, C. Ghica, B. G. Almeida, L. Marques, M. Pereira, J. P. B. Silva, Phase transitions and ferroelectric properties in ZrO_2 thin films (under review).
[38] K. Chae, S. F. Lombardo, N. Tasneem, M. Tian, H. Kumarasubramanian, J. Hur, W. Chern, S. Yu, C. Richter, P. D. Lomenzo, M. Hoffmann, U. Schroeder, D. Triyoso, S. Consiglio, K. Tapily, R. Clark, G. Leusink, N. Bassiri-Gharb, P. Bandaru, J. Ravichandran, A. Kummel 1, K. Cho, J. Kacher, A. I. Khan, *ACS Appl. Mater. Interfaces.* **2022**, *14*, 36771.
[39] B. Xu, P. D. Lomenzo, A. Kersch, T. Mikolajick, U. Schroeder, *ACS Appl. Electron. Mater.* **2022**, *4*, 3648.
[40] S. Shibayama1, J. Nagano, M. Sakashita, O. Nakatsuka, *Jpn. J. App. Phys.* **2020**, *59*, SMMA04.
[41] S. Starschich, T. Schenk, U. Schroeder, U. Boettger, *Appl. Phys. Lett.* **2017**, *110*, 182905.

© 2023 The Authors. Advanced Science published by Wiley-VCH GmbH

21983844, 2023, 15, Downloaded from https://onlinelibrary.wiley.com/doi/10.1002/advs.202207390 by Cochrane Portugal, Wiley Online Library on [26/07/2023]. See the Terms and Conditions (https://onlinelibrary.wiley.com/terms-and-conditions) on Wiley Online Library for rules of use; OA articles are governed by the applicable Creative Commons License